Experimental and theoretical study on the excited-state dynamics of ortho-, meta-, and para-methoxy methylcinnamate

Yasunori Miyazaki, Kanji Yamamoto, Jun Aoki, Toshiaki Ikeda, Yoshiya Inokuchi, Masahiro Ehara, and Takayuki Ebata

---

Articles you may be interested in

Excited-state intramolecular proton transfer reaction modulated by low-frequency vibrations: An effect of an electron-donating substituent on the dually fluorescent bis-benzoxazole
J. Chem. Phys. **135**, 034307 (2011); 10.1063/1.3609759

On the origin of ultrafast nonradiative transitions in nitro-polycyclic aromatic hydrocarbons: Excited-state dynamics in 1-nitronaphthalene
J. Chem. Phys. **131**, 224518 (2009); 10.1063/1.3272536

Ultrafast excited-state dynamics of tetraphenylethylene studied by semiclassical simulation
J. Chem. Phys. **127**, 094307 (2007); 10.1063/1.2768347

Combined experimental-theoretical study of the lower excited singlet states of paravinyl phenol, an analog of the paracoumaric acid chromophore
J. Chem. Phys. **125**, 204303 (2006); 10.1063/1.2366702

Geometries and excited-state dynamics of van der Waals dimers and higher clusters of 1-cyanonaphthalene
J. Chem. Phys. **123**, 244306 (2005); 10.1063/1.2141613

Experimental and theoretical study on the excited-state dynamics of *ortho-*, *meta-*, and *para*-methoxy methylcinnamate

Yasunori Miyazaki,[1] Kanji Yamamoto,[1] Jun Aoki,[1] Toshiaki Ikeda,[1] Yoshiya Inokuchi,[1] Masahiro Ehara,[2,3] and Takayuki Ebata[1,a)]

[1]*Department of Chemistry, Graduate School of Science, Hiroshima University, Higashi-Hiroshima 739-8526, Japan*
[2]*Institute for Molecular Science and Research Center for Computational Science, 38 Myodaiji, Okazaki 444-8585, Japan*
[3]*Elements Strategy for Catalysts and Batteries, Kyoto University, Katsura, Kyoto 615-8520, Japan*
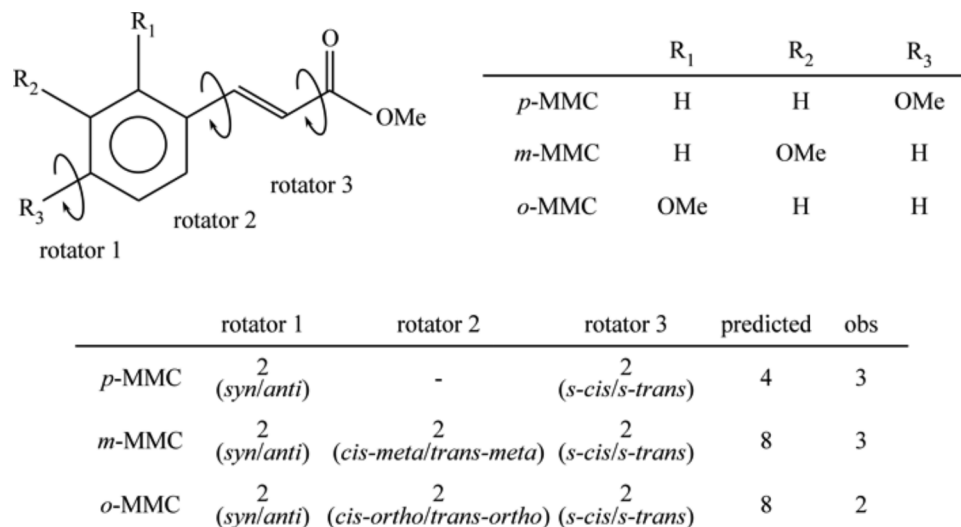
The S_1 state dynamics of methoxy methylcinnamate (MMC) has been investigated under supersonic jet-cooled conditions. The vibrationally resolved S_1-S_0 absorption spectrum was recorded by laser induced fluorescence and mass-resolved resonant two-photon ionization spectroscopy and separated into conformers by UV-UV hole-burning (UV-UV HB) spectroscopy. The S_1 lifetime measurements revealed different dynamics of *para*-methoxy methylcinnamate from *ortho*-methoxy methylcinnamate and *meta*-methoxy methylcinnamate (hereafter, abbreviated as *p*-, *o*-, and *m*-MMCs, respectively). The lifetimes of *o*-MMC and *m*-MMC are on the nanosecond time scale and exhibit little tendency of excess energy dependence. On the other hand, *p*-MMC decays much faster and its lifetime is conformer and excess energy dependent. In addition, the *p*-MMC-H_2O complex was studied to explore the effect of hydration on the S_1 state dynamics of *p*-MMC, and it was found that the hydration significantly accelerates the nonradiative decay. Quantum chemical calculation was employed to search the major decay route from $S_1(\pi\pi^*)$ for three MMCs and *p*-MMC-H_2O in terms of (i) *trans* → *cis* isomerization and (ii) internal conversion to the $^1n\pi^*$ state. In *o*-MMC and *m*-MMC, the large energy barrier is created for the nonradiative decay along (i) the double-bond twisting coordinate ($\sim$1000 cm^{-1}) in S_1 as well as (ii) the linear interpolating internal coordinate ($\sim$1000 cm^{-1}) from S_1 to $^1n\pi^*$ states. The calculation on *p*-MMC decay dynamics suggests that both (i) and (ii) are available due to small energy barrier, i.e., 160 cm^{-1} by the double-bond twisting and 390 cm^{-1} by the potential energy crossing. The hydration of *p*-MMC raises the energy barrier of the IC route to the S_1/$^1n\pi^*$ conical intersection, convincing that the direct isomerization is more likely to occur. © *2014 AIP Publishing LLC.* [http://dx.doi.org/10.1063/1.4904268]

I. INTRODUCTION

Plants rely on cinnamate in a wide range of physiological activities. It is believed that cinnamate is an important secondary metabolite in plant growth and development.[1,2] Lignin, synthesized by polymerization of *p*-coumaryl, coniferyl, and sinapyl alcohols, which are all modified from *p*-coumaric acid, controls not only flexibility of cell wall but also structural rigidity.[3–7] In addition to the resistance to mechanical stress, it provides protection against microbial infection that breaks down polysaccharide into single sugar components.[8–10] The conjugated alkene in the cinnamate skeleton also has a pivotal role in UV filter that protects photodegradation of DNA and photosensitive molecules by *trans-cis* isomerization.[11,12] Such UV absorbing compound has been given attention in cosmetic market to reduce risk of the skin damage when exposed to the sunlight.[13,14] The comparative studies of various cinnamate derivatives in the condensed phase addressed that nonradiative decay is strongly dependent upon the substituent and the position in the aromatic ring.[15–18] For example, *para*-methoxy

methylcinnamate has low fluorescence quantum yield, which is to say a short S_1 lifetime, suggesting that it is quite useful for UV screening. Ehara and his coworkers employed an advanced *ab initio* calculation to draw the potential energy curve of *ortho-*, *meta-*, and *para*-substituted hydroxy methylcinnamate (HMC) and methoxy methylcinnamate (MMC) along the C=C isomerization coordinate and provided the quantitative evaluation of their energy barrier heights,[19,20] which are in good agreements with their behaviors of the $S_1(\pi\pi^*)$ state. Therefore, they concluded that the nonradiative decay of cinnamate proceeds by the double bond twisting. Conversely, Buma and his coworkers have proposed another decay mechanism since they studied jet-cooled OM*p*CA (methyl-4-hydroxycinnamate) and found a 29 ns long-lived excited state after the molecule was pumped to the $S_1(\pi\pi^*)$ state,[21] although the $S_1(\pi\pi^*)$ state itself has a lifetime of as short as 9 ps.[22] Recently, they reported that *p*-MMC undergoes a similar excited state dynamics to OM*p*CA where an intermediate is repopulated with the lifetime of 24 ns.[23] Based on the spectroscopic observation and the theoretical calculation, they assigned it to the $^1n\pi^*$ state and argued that OM*p*CA and *p*-MMC decay mainly by internal conversion (IC).[21,23,24] The nonradiative decay dynamics of cinnamate is now known

---

a)Author to whom correspondence should be addressed. Electronic mail: tebata@hiroshim-u.ac.jp

	R_1	R_2	R_3
p-MMC	H	H	OMe
m-MMC	H	OMe	H
o-MMC	OMe	H	H

	rotator 1	rotator 2	rotator 3	predicted	obs
p-MMC	2 (*syn/anti*)	-	2 (*s-cis/s-trans*)	4	3
m-MMC	2 (*syn/anti*)	2 (*cis-meta/trans-meta*)	2 (*s-cis/s-trans*)	8	3
o-MMC	2 (*syn/anti*)	2 (*cis-ortho/trans-ortho*)	2 (*s-cis/s-trans*)	8	2

SCHEME 1. Molecular structure (top) and specified conformation (bottom) of MMC.

to be sensitive to the methyl-ester functional group[25] and combination of the substituents in the ring.[26]

In this article, keeping above studies in mind, we study the S_1 state dynamics of *ortho*-, *meta*-, and *para*-methoxy methylcinnamate (abbreviated as *o*-MMC, *m*-MMC, and *p*-MMC, respectively) under jet-cooled conditions in the gas phase. Taking an advantage of jet-cooling, the effect of substitution in the aromatic ring is reconfirmed by collecting the lifetime of the S_1 vibronic levels for the distinct conformer of MMCs (Scheme 1) and calculating the double bond twisting and $S_1(\pi\pi^*)$-$^1n\pi^*$ potential energy curve crossing. Of all, we are interested in *p*-MMC, especially how its nonradiative process is affected by the hydration, because our previous study of OM*p*CA showed a surprising elongation of the S_1 lifetime by a factor of 100 as a result of the hydration to the phenolic OH group.[22] In the case of *p*-MMC, the hydration site is only restricted to the carbonyl oxygen. It is expected that the partially stabilized non-bonding energy level increases the transition energy of the $^1n\pi^*$ state. The fate of the S_1 state dynamics in the *p*-MMC-H$_2$O complex is described by lifetime measurement and two nonradiative decay models.

II. METHODOLOGY

A. Experimental setup

Details of the experimental setup were described elsewhere.[22] Briefly, *p*-MMC (solid sample), *o*-MMC (liquid sample), or *m*-MMC (liquid sample) in the sample house located at the head of a pulsed nozzle was vaporized at 100-120 °C by heating and diluted with He carrier gas at a total pressure of 1.5 bars. The mixture of gaseous samples was expanded into vacuum through a 1 mm orifice of the pulsed nozzle. The S_1-S_0 electronic spectrum was recorded by laser induced fluorescence (LIF) and mass-resolved resonant two-photon ionization (R2PI) spectroscopies. In the LIF measurement, a tunable UV laser was generated by second harmonics generation (SHG) of an output of the Nd^{3+}:YAG laser pumped dye laser (Lambda Physik Scanmate/Continuum Surelite II), which was operating

with Rhodamin 640 for *p*-MMC and a mixture of DCM and Rhodamin 640 for *m*-MMC and *o*-MMC, and introduced into the vacuum chamber to cross the supersonic free jet at ~20 mm downstream of the orifice. The LIF spectrum was obtained by detecting the total fluorescence with a photomultiplier tube as a function of the UV frequency. The mass-resolved R2PI measurement was performed by using another vacuum chamber containing a molecular beam system; the molecules in a molecular beam which was produced by skimming the free jet expansion were ionized by R2PI via the S_1 state, and the ions were mass-selected by the reflectron time-of-flight (TOF) spectrometry and detected with a multichannel plate (MCP) detector. The R2PI spectrum was obtained by plotting the mass-selected ion signal as a function of the UV frequency. UV-UV hole-burning (UV-UV HB) spectroscopy was carried out to discriminate bands belonging to different isomers. The probe UV laser was fixed to the vibronic band of interest and its fluorescence intensity was monitored. Under this condition, another tunable UV laser (hole laser) generated by SHG of the Nd^{3+}:YAG laser pumped dye laser (Continuum ND6000/ Surelite II) was introduced at 10 mm upstream of the crossing point between the jet and the probe laser at ~4 μs prior to the probe laser pulse. A depletion of the fluorescence intensity was observed due to ground state depopulation induced by the hole laser. Thus, the UV-UV HB spectra were recorded as dip spectra. The IR-UV double resonance (IR-UV DR) spectroscopic measurement was performed by a molecular beam machine; an output of a pulsed tunable IR laser (Laser Vision/Quanta-Ray GCR250) was used as a pump laser. The IR laser was introduced coaxially to the probe UV laser with an interval of 80 ns prior the UV pulse. UV probe laser frequency was fixed to the vibronic band of the S_1-S_0 transition and the IR laser frequency was scanned. A depletion of the ion signal induced by the IR pump laser was detected, giving ion-dip IR spectra for the UV monitored species.

For the species with its S_1 lifetime shorter than a few nanoseconds, picosecond pump-probe spectroscopy was employed. The setup of the picosecond pump-probe laser system has been also described in detail elsewhere.[22] Briefly,

a mode-locked picosecond Nd^{3+}:YAG laser (Ekspla PL2143S) was use to pump two optical parametric generation/optical parametric amplifier (OPG/OPA) systems (Ekspla PG401 SH) and frequency doubled to generate a tunable UV laser pulse. The spectral and time resolutions of the UV laser pulse were $5 \ cm^{-1}$ and 12 ps, respectively. Two UV lasers were introduced to cross the molecular beam in a counter-propagated manner and ionized the molecule or complex in the molecular beam by a stepwise two-photon ionization. The ions were mass-analyzed with a 50 cm time-of-flight tube and were detected by a channeltron (Burle 4900). The decay time profile of the S_1 state was obtained by measuring pump–probe ion signals as a function of the delay time between the pump and probe UV laser pulses, which was controlled by an optical delay line. The ion signals were processed by a boxcar integrator (Par model 4401/4420) connected to PC. The decay time constants were analyzed by deconvolution method. For the species of its S_1 lifetime longer than a few nanoseconds, the lifetime was determined by deconvoluting the time profile of the fluorescence decay curve with assumption that the laser pulse was 5.0 ns width of the Gauss function. The uncertainty of the obtained S_1 lifetime is estimated to be 15%. All the samples were synthesized (see sample preparation in the supplementary material[34]) and were used without further purification.

B. Computational detail

The experimental result was described by *ab initio* and DFT calculations using Gaussian 09 program.[27] The S_0 state geometry optimization of MMCs was performed by the DFT/PBE0 calculation[28] with the cc-pVDZ basis set.[29] The *p*-MMC conformers were all optimized in the C_s symmetry and the observed species in the UV-UV HB spectrum were assigned by comparing (i) the relative band intensity in the R2PI spectrum with the calculated stabilization energy in the S_0 state and (ii) the electronic transition energies in the R2PI spectrum with the calculated vertical excitation energies without zero-point energy correction. The numbers of possible conformations of *m*-MMC and *o*-MMC are 8 and 4, respectively, both having the C_s symmetry (see Fig. S1 of the supplementary material for the structures[34]). The number of *o*-MMC conformers is reduced to half because *cis-ortho* conformer does not converge into their local minima due to the repulsive interaction between O-CH$_3$ and propenyl C-H at the rotator 1 (Scheme 1). The S_0 state of the *p*-MMC-H_2O complex was optimized in the manner that one OH group of water is hydrogen-bonded to the carbonyl oxygen as a proton donor and the other one tilts to form a bridge with the CH of either the propenyl group or the methyl ester group. The calculated OH stretch frequencies of the C_1-symmetrized complex were compared to the observed ones in the IR-UV DR spectra. The various complex structures where the water molecule is bounded to the methoxy oxygen, ester oxygen, and aromatic ring are illustrated in supplementary material (see Figs. S2 and S3 of the supplementary material[34]).

Two kinds of electronic excited-state calculations were carried out to assess the nonradiative decay routes from the $S_1(\pi\pi^*)$ state for three MMCs as well as the water complex of *p*-MMC. One is the IC route through the potential energy curve crossing. The geometry optimizations for three excited states (S_1, S_2, and S_3) of MMCs including the water complex were performed within the C_s symmetry by the TD-PBE0/cc-pVDZ level of theory. The energy of these states was calculated at each intermediate structure and plotted as a linear interpolation internal coordinate (LIIC). The other is the direct *trans-cis* isomerization route. The potential energy curve along the dihedral angle was obtained by the CIS(D)/aug-cc-pVDZ calculation.[30] For the geometry, the partial optimization of the $S_1(\pi\pi^*)$ state was performed at the dihedral angle varying from 180° to 140° with a step of 10° at the propenyl double-bond using the CIS/aug-cc-pVDZ calculation with all the other coordinates being optimized. These methods with selected basis sets interpret the experimental observation well.

III. RESULTS

A. S_1-S_0 electronic excitation spectrum of jet-cooled *p*-MMC

Figs. 1(a) and 1(b) show the LIF and R2PI spectra recorded in the S_1-S_0 transition region of *p*-MMC, respectively. Our spectra are essentially the same as the reported one.[23] An identical vibronic structure was obtained between the LIF and R2PI spectra except the difference of the relative band intensity. The weakening band intensity in the higher energy region of the LIF spectrum is ascribed to the shortening of the S_1 lifetime, as will be discussed in Sec. III B. Since the R2PI spectrum was recorded by using laser power stronger than LIF spectrum, several extra bands which were assigned to hot bands (marked by asterisks) appeared and some of the vibronic bands were broadened due to saturation. The UV frequency and band intensity of the major vibronic band are listed in Table I. UV-UV HB spectroscopy was employed to clarify the overlapping spectra in the R2PI spectrum with the probe laser frequency fixed at $32\,328 \ cm^{-1}$, $32\,587 \ cm^{-1}$, and $32\,667 \ cm^{-1}$ in Figs. 1(c)–1(e), respectively. It is obvious that the R2PI spectrum is composed of the bands in the three UV-UV HB spectra. Tan *et al.* discriminated only two species with their S_1-S_0 origins at $32\,328 \ cm^{-1}$ and $32\,667 \ cm^{-1}$ and attributed them to *s-cis* and *s-trans* conformers, respectively.[23] Here, we analyzed our UV-UV HB spectra carefully and reassigned them with the aid of DFT calculation.

Given that the conformation is specified by the rotator 1 (*syn* and *anti*) and the rotator 3 (*s-cis* and *s-trans*) in Scheme 1, *p*-MMC is expected to have four conformers in total. Their DFT calculated molecular structures and relative S_0 energies including the zero-point energy correction are shown in Fig. 2.

The *s-cis/anti* is the most stable conformer of all and the rest have the energies within $403 \ cm^{-1}$. Based on their optimized structures, the TD-PBE0 calculation was employed to validate their S_1-S_0 electronic transition energies, as depicted in Fig. 1(f). This result indicates that the four conformers have different UV transition energies from one another. In fact, the S_1-S_0 electronic spectrum of anethole ((E)-1-methoxy-4-(1-propenyl)benzene) is discriminated into the *syn*- and *anti*-conformers with their 0-0 bands at $32\,889 \ cm^{-1}$
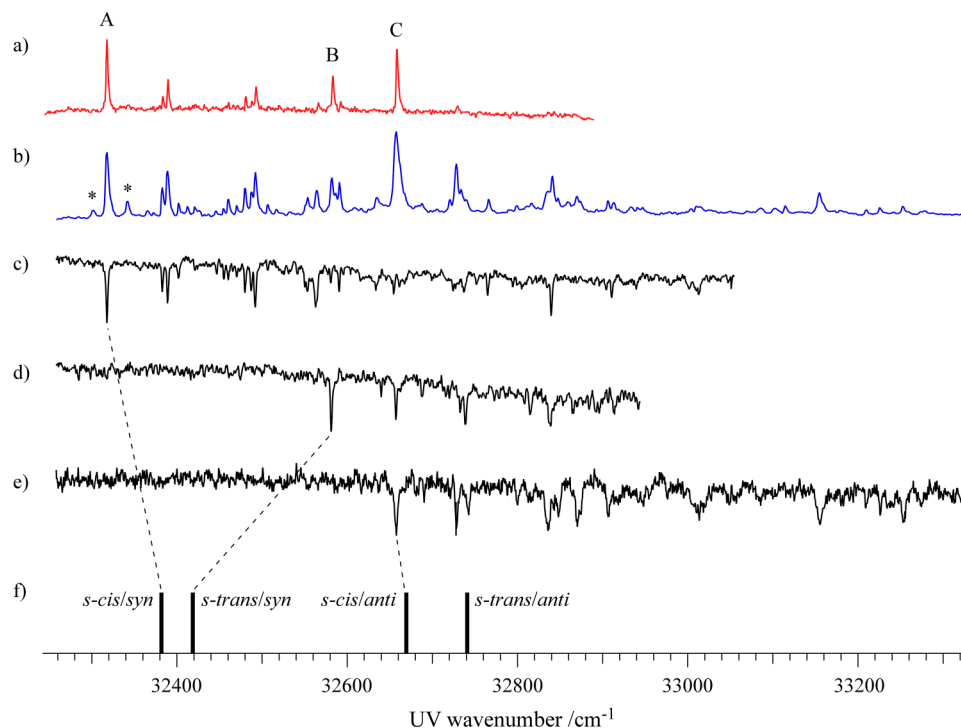
FIG. 1. (a) LIF spectrum and (b) mass-selected R2PI spectrum of jet-cooled *p*-MMC. Asterisks (*) indicate hot bands around the S_1-S_0 band origin. Some of the bands in the R2PI spectrum were broadened by saturation due to rather stronger laser power than the LIF spectrum. (c)–(e) UV-UV HB spectra of *p*-MMC recorded at the band A (32 328 cm^{-1}), band B (32 587 cm^{-1}), and band C (32 667 cm^{-1}), respectively, to show the coexisted conformers in the R2PI spectrum. (f) TD-PBE0 calculated electronic transition energies of *s-cis/syn*, *s-trans/syn*, *s-cis/anti*, and *s-trans/anti* conformers.

and 32 958 cm^{-1}, respectively, giving the energy separation of 69 cm^{-1}.[31] Therefore, the observed species are ascribed to three distinct conformers out of four conformers and we assigned them by comparing (i) the calculated relative S_0 energies with the R2PI intensities and (ii) the calculated S_1-S_0 electronic transition energies with the UV frequencies of the observed 0-0 bands. For instance, band C was assigned to the *s-cis/anti* conformer as it shows the strongest band intensity and appears at the highest frequency among three

species in the R2PI spectrum. The former corresponds to the most populated conformer in the supersonic jet expansion, which turns out to be the most stable one in the calculation, and the latter is in accord with the vertical excitation energy. Similarly, band A is assigned to the *s-cis/syn* conformer and band B is assigned to the *s-trans/syn* conformer by following the same argument as above. It should be noted that the R2PI intensity depends not only on the ground sate population but also on the Franck-Condon Factors (FCFs) of the S_1-S_0

TABLE I. Position of the observed bands of *p*-MMC in cm^{-1}, relative energies from the band origin in cm^{-1}, relative band intensities in the R2PI spectrum, conformer assignment, and S_1 lifetime in ps. The uncertainty of the lifetimes is 15%.

Transition energy (cm^{-1})	Relative transition energy (cm^{-1})	Relative intensity	Assignment (cm^{-1})	S_1 lifetime (ps)
32 328	0	81	*s-cis/syn* (0,0)	280
32 383	65	40	*s-cis/syn* + 65	
32 389	71	60	*s-cis/syn* + 71	190
32 480	162	39	*s-cis/syn* + 162	
32 492	174	58	*s-cis/syn* + 174	85
32 554	236	29	*s-cis/syn* + 236	
32 564	246	37	*s-cis/syn* + 246	
32 582	264	51	*s-trans/syn* (0,0)	108
32 591	273	46	*s-cis/syn* + 273	
32 667	340	100	*s-cis/anti* (0,0)	80
32 728	410	57	*s-cis/anti* + 70	34
32 766	448	26	*s-cis/syn* + 448	
32 841	523	54	*s-cis/anti* + 183	13
33 155	837	34	*s-cis/anti* + 497	

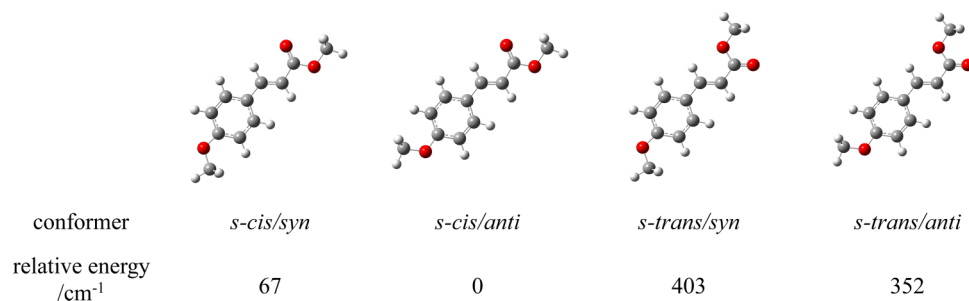| conformer	*s-cis/syn*	*s-cis/anti*	*s-trans/syn*	*s-trans/anti*
relative energy /cm^{-1}	67	0	403	352

FIG. 2. Four conformers of *p*-MMC and their relative S_0 energies calculated at the PBE0/cc-pVDZ level. The conformation is specified by the single bond rotation of methoxy group (*syn* and *anti*) and the orientation of propenyl double bond with respect to the carbonyl group (*s-cis* and *s-trans*).

transition and the lifetime of the S_1 intermediate state. In the present system, all the four conformers are planar in S_0 and S_1 so that the FCFs can be assumed to be similar among them. The effect of the S_1 lifetime on the R2PI intensity is most important for band C (*s-cis/anti* conformer) because band C has the shorter S_1 lifetime than band A and band B. However, including the S_1 lifetime will result in the more stabilization energy for this conformer so that the assignment of band C to the most stable conformer is unchanged. The *s-trans/anti* conformer is predicted to appear at the higher frequency region than the band C but its band intensity seems to be very weak. This is because this conformer has the second highest S_0 energy and its S_1 lifetime seems to be very short as will be discussed in Sec. III B.

B. S_1 lifetime measurement of *p*-MMC

Fig. 3(a) shows the picosecond pump-probe decay time profile of *p*-MMC recorded at the S_1-S_0 band origin and associated vibronic bands of the *s-cis/syn*, *s-trans/syn*, and *s-cis/anti* conformers. A single exponential decay curve was required to fit all decay time profiles that yield the S_1 lifetime as listed in Table I. In contrast to the estimated lifetimes from the bandwidth analysis of the S_1-S_0 vibronic bands,[23] our lifetime measurement gave much longer lifetimes on a picosecond time scale. Furthermore, the S_1 lifetime is strongly conformer dependent, i.e., 280 ps for *s-cis/syn*, 108 ps for *s-trans/syn*, and

80 ps for *s-cis/anti* at their 0-0 band origins. Each conformer exhibits the excess energy dependence of S_1 lifetime, suggesting the existence of potential energy barrier for the nonradiative decay. Fig. 3(b) shows the plot of the decay rate constant k ($=1/\tau$) as a function of the UV excitation energy, providing more clear picture of *p*-MMC S_1 lifetime that is both excess energy and conformer dependent.

C. R2PI and IR-UV DR spectra of *p*-MMC-H$_2$O

Fig. 4(a) shows the S_1-S_0 R2PI spectra of *p*-MMC monomer (upper panel) and the mass-selected *p*-MMC-H$_2$O complex (lower panel). The S_1-S_0 transition of the water complex is 130 ~ 200 cm^{-1} red-shifted from the monomer, which agrees with the recently reported R2PI spectrum.[23] Tan *et al.* found four species that coexist in the jet-cooled R2PI spectrum by means of UV-UV HB spectroscopy, but they did not determine the hydrated structure. Thus, we measured the IR-UV DR spectra of the *p*-MMC-H$_2$O complex by fixing the UV frequency at the prominent bands **a′** and **b′**. Fig. 4(b) displays the IR spectra recorded by monitoring the band **a′** (32 106 cm^{-1}, upper panel) and the band **b′** (32 529 cm^{-1}, lower panel). In general, they share the same spectral features. In the IR spectrum of the band **a′**, the observed frequency at 3540 cm^{-1} is the hydrogen(H)-bonded OH stretch vibration of H$_2$O, and the weak one located at 15 cm^{-1} higher frequency is assigned to the combination band
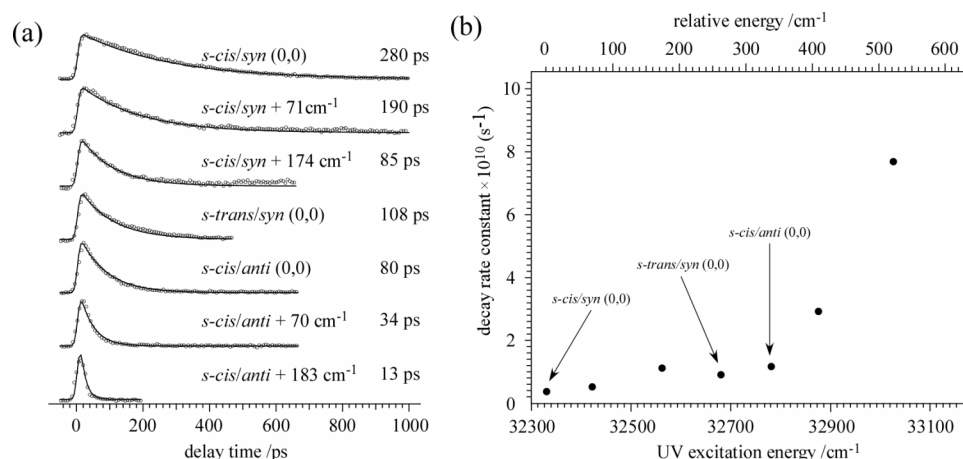

FIG. 3. (a) Pump-probe ion signal (circle) and decay time profile (solid line) of *p*-MMC at the S_1-S_0 band origin and associated vibronic levels of the *s-cis/syn*, *s-trans/syn*, and *s-cis/anti* conformers. (b) Plot of decay rate constant of *p*-MMC vs the UV excitation energy.
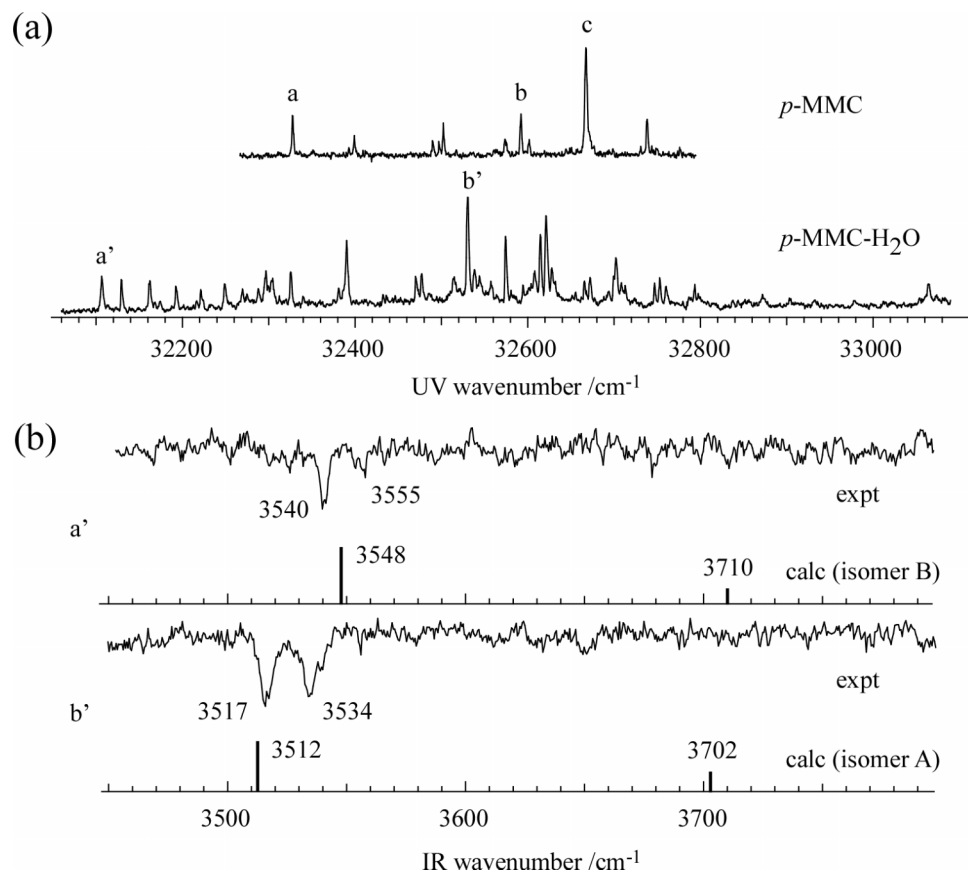
FIG. 4. (a) R2PI spectrum of *p*-MMC (top) and *p*-MMC-H$_2$O (bottom) recorded by using the nanosecond laser system. The labels a–c indicate the S$_1$-S$_0$ band origin of the *p*-MMC conformer. The labels a′ and b′ are the S$_1$-S$_0$ band origins of *p*-MMC-H$_2$O isomers where the H$_2$O moiety is bounded at two different sites of the carbonyl oxygen as evidenced by IR-UV DR spectroscopy (read text). (b) IR-UV DR spectra of *p*-MMC-H$_2$O with the probe laser fixed at 32 106 cm^{-1} (**a′**, upper panel) and 32 529 cm^{-1} (**b′**, lower panel). The stick in the spectrum is the calculated OH stretch frequency by PBE0/cc-pVDZ and corrected with a scaling factor of 0.955.

of the OH stretch coupled with the intermolecular vibration. In the IR spectrum of the band **b′**, two bands appeared with almost equal intensity. The bands at 3517 cm^{-1} and 3534 cm^{-1} were assigned to the H-bonded OH stretch of H$_2$O and the combination band with the intermolecular vibration, respectively. Because the H-bonded OH stretch frequency of the band **a′** is different from the band **b′**, these species are considered to be isomers having a different H-bonding structure.

So, we calculated the structure of the *p*-MMC-H$_2$O complex with a fixed conformation of *p*-MMC site but different H-bonding binding sites. Fig. 5 shows the two lowest energy isomers of the *s-cis/anti p*-MMC-H$_2$O complex. The structures and IR spectra of other higher energy isomers are illustrated in supplementary material (see Figs. S2 and S3 of the supplementary material[34]). As shown in Fig. 5, isomer A and isomer B were optimized with the water molecule binding at two hydration sites of the carbonyl oxygen of the *s-cis/anti p*-MMC conformer (the lowest energy conformation). That is, the OH group of water is hydrogen-bonded to the carbonyl oxygen as a proton donor and the water oxygen is weakly bounded to either CH of the propenyl group (isomer A) or CH of methyl ester group as a proton acceptor (isomer B). According to the calculation, isomer A is much more stabilized in energy than isomer B due to more attractive

interaction of OH⋯H–C=C than OH⋯H–C–O, which also reflects their bond lengths and IR frequency. Thus, isomer A has the hydrogen-bonded OH stretch frequency lower than isomer B (Fig. 4(b)), which meets a good agreement with the observation. The free OH stretch of water at around 3710 cm^{-1} was not observed due to that the signal-to-noise ratio was not good enough to detect the weak IR band. From these results, we assigned the species of band **a′** to isomer B and that of band **b′** to isomer A.

D. S$_1$ lifetime measurement of *p*-MMC-H$_2$O

Fig. 6 shows the decay time profiles of the *p*-MMC-H$_2$O complex measured for band **a′** (32 106 cm^{-1}, left) and band **b′** (32 529 cm^{-1}, right) by picosecond pump-probe spectroscopy. Deconvolution with the least square fitting of a double-exponential decay curve yielded the lifetime for the fast and slow components, i.e., $\tau_1 = 21$ ps and $\tau_2 = 150$ ps for band **a′**, and $\tau_1 = 35$ ps and $\tau_2 = 150$ ps for band **b′**. In both cases, the coefficient of the slow component is much smaller than the fast one. The noticeable point is that the lifetime of the fast component, whichever water is bounded to propenyl double bond (**b′**) or methyl ester (**a′**), is much shorter than the monomer (such as 280 ps, 108 ps, and 80 ps). These results lead us the conclusion that the hydration to the
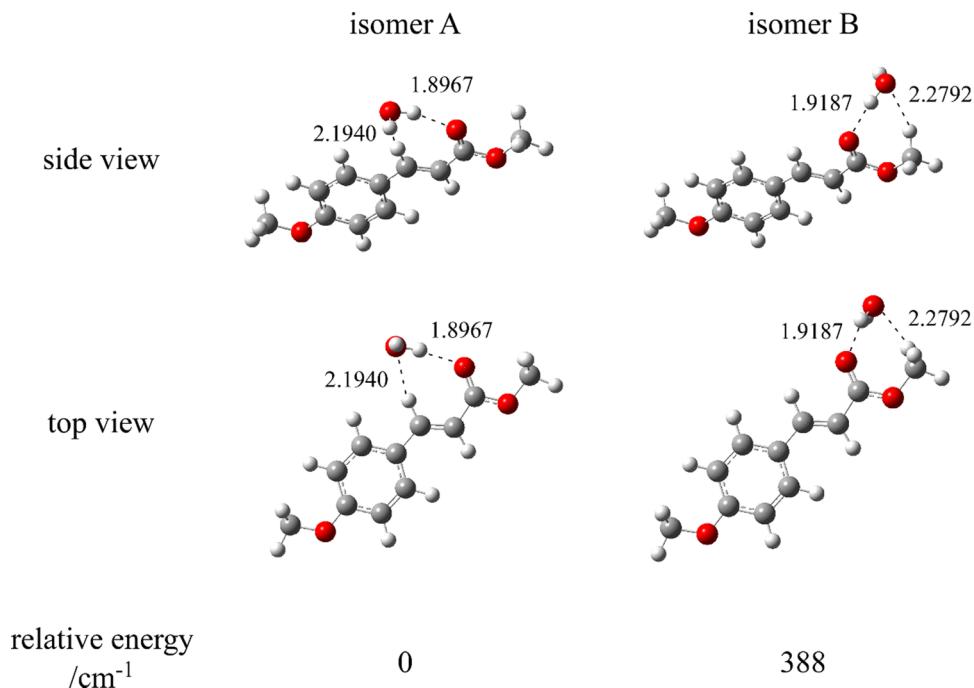
isomer A   isomer B

FIG. 5. Isomer A and isomer B of *s-cis/anti p*-MMC-H$_2$O complex optimized at the PBE0/cc-pVDZ level of theory and relative S$_0$ energies including the zero-point energy correction.

carbonyl group accelerates the nonradiative decay process of *p*-MMC.

E. Electronic excitation spectra and S$_1$ lifetime of *m*-MMC and *o*-MMC

Fig. 7(a) displays the LIF spectrum of jet-cooled *m*-MMC (red trace) recorded in the region between 31 000 cm^{-1} and 32 230 cm^{-1}. One-color R2PI spectrum could not be obtained probably due to the reason that the ionization potential (IP$_0$) of this molecule is larger than twice of the S$_1$-S$_0$ transition energy, so that one-color two-photon energy does not reach to IP$_0$. In order to determine the number of conformations, UV-UV HB spectra were recorded by monitoring the band A (31 120 cm^{-1}), the band B (31 310 cm^{-1}), and the band C (31 340 cm^{-1}) as shown in Fig. 7 (black traces). The asterisk (*) at 31 481 cm^{-1} is also considered to be one of the conformers though the band intensity is too weak to record its UV-UV HB spectrum. Therefore, at least four conformers coexist in the LIF spectrum.

A full conformational assignment was not carried out due to the lack of concrete spectroscopic evidence to support the assignment (see Fig. S1(a) of the supplementary material[34] for optimized conformations and relative S$_0$ energies). The S$_1$ lifetime of each band was estimated by deconvolution of the fluorescence decay profile that yielded 27, 15, and 16 ns at the band A, B, and C, respectively. The other vibronic bands have the lifetimes in the range of 15–16 ns. Little energy dependence was observed even at 800 cm^{-1} above the S$_1$-S$_0$ band origin, suggesting that *m*-MMC has potential energy barrier higher than *p*-MMC and the radiative decay is preferred.

Fig. 7(b) displays the S$_1$-S$_0$ LIF spectrum (red trace) and UV-UV HB spectra (black traces) of jet-cooled *o*-MMC recorded in the region between 30 710 cm^{-1} and 32 100 cm^{-1}. One-color R2PI spectrum was not obtainable probably due to the same reason as *m*-MMC. All transitions were ascribed to two conformers with the S$_1$-S$_0$ band origin at 30 738 cm^{-1} (conformer A) and at 30 746 cm^{-1} (conformer B), respectively, though conformer A is a minor species. As with
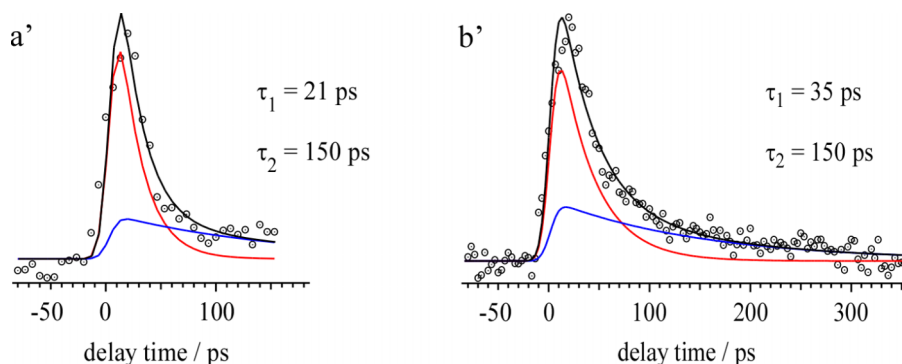

FIG. 6. Pump-probe ion signals (dotted circle) and best-fitted decay time profiles (red: fast component, blue: slow component, black: sum of two components) of the *p*-MMC-H$_2$O complex measured at the band **a′** (left, 32 106 cm^{-1}) and the band **b′** (right, 32 529 cm^{-1}).
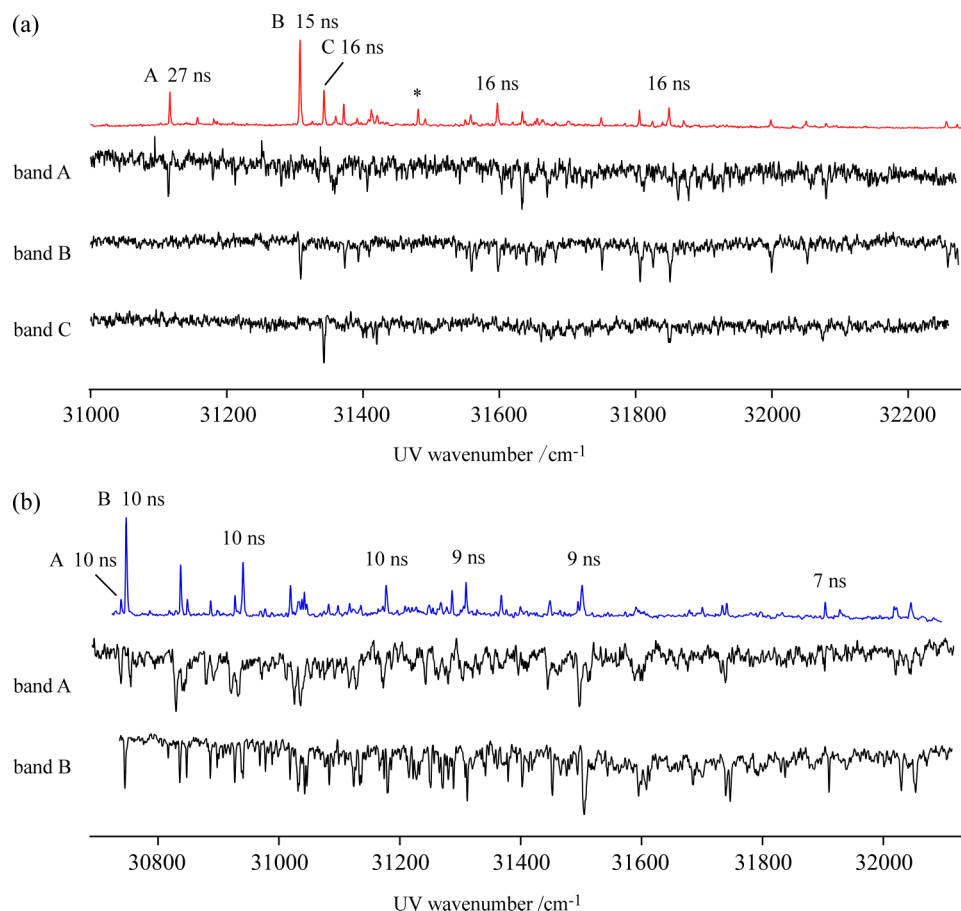
FIG. 7. (a) The S_1-S_0 LIF spectrum (red trace) of m-MMC and UV-UV HB spectra (black traces) by monitoring the bands A, B, and C. (b) The S_1-S_0 LIF spectrum (blue trace) of o-MMC and UV-UV HB spectra (black traces) by monitoring the bands A and B. The number written above each band is the S_1 lifetime in unit of ns. The uncertainty of the lifetimes is 15%.

m-MMC, a full conformational assignment was not carried out (see supplementary material Fig. S1(b)[34] for optimized conformations and relative S_0 energies). The S_1 lifetime of o-MMC was estimated in the range of 7–10 ns in the S_1-S_0 excitation region. It indicates that o-MMC also has a large energy barrier to overcome for nonradiative decay. These results meet a good agreement with the fluorescent lifetime measured in the condensed phase.[15]

IV. DISCUSSION

A. Nonradiative decay route of *p*-MMC

In this section, nonradiative decay route of MMCs is examined to describe the experimental results by two theoretical calculations. One route is the IC. Gromov *et al.* pointed out the reversed order of the energy levels of the $S_1(\pi\pi^*)$ and $^1n\pi^*$ states in coumaric acid when the vertical and adiabatic excitation energies are calculated; the $S_1(\pi\pi^*)$ state is lower in vertical excitation energy than the $^1n\pi^*$ state while adiabatically the $^1n\pi^*$ state is lower than the $S_1(\pi\pi^*)$ state.[24] Buma and his coworkers persisted that the $S_1(\pi\pi^*) \rightarrow {}^1n\pi^*$ IC is favorable since they found an excited state having rather long lifetime, i.e., 29 ns for OMpCA[21] and 24 ns for p-MMC[23] by the nanosecond pump-probe experiment using the 193 nm ionization. They proposed that this long-lived excited state

is the $^1n\pi^*$ state. Second nonradiative route is the decay via the double bond twisting (*trans $\rightarrow$ cis* isomerization) in the $S_1(\pi\pi^*)$ potential energy surface. It was suggested by Ehara and his coworkers from their potential energy calculations along the C=C double bond rotational coordinate for p-, m-, and o-MMCs.[19] In our previous paper, we supported this mechanism to describe the lifetime elongation of OMpCA upon the hydration to the phenolic OH group.[22]

B. IC from the $S_1(\pi\pi^*)$ state to the $^1n\pi^*$ state

We first calculated the vertical and adiabatic energies of three electronic excited states, i.e., $1A'(^1\pi\pi^*)$, $1A''(^1n\pi^*)$, and $2A'(^1\pi\pi^*)$ states, for p-, m-, and o-MMCs. The results are summarized in Table II, where the energies were obtained without the zero-point energy correction. The geometrical changes of each electronic excited state relative to S_0 are given in supplementary material (see Figs. S4–S6 of the supplementary material[34]). As seen in Table II, $1A'(\pi\pi^*)$ is the lowest in vertical excitation energy and corresponds to S_1. $1A''(^1n\pi^*)$ is the second lowest in vertical excitation energy and corresponds to S_2. The vertical excitation energy of $2A'(^1\pi\pi^*)$ is even higher than those and it can be excluded from the nonradiative decay process initiated from the S_1 state (see Fig. S7 of the supplementary material to verify the uninvolved $2A'(^1\pi\pi^*)$[34]). The order of the electronic excited

TABLE II. Vertical and adiabatic transition energies of the S_1, S_2, and S_3 states of *o*-, *m*-, and *p*-MMCs calculated at TD-PBE0/cc-pVDZ. The zero-point energy correction is not included.

	Vertical (eV)			Adiabatic (eV)		
	1A′($\pi\pi^*$)	1A″($n\pi^*$)	2A′($\pi\pi^*$)	1A′($\pi\pi^*$)	1A″($n\pi^*$)	2A′($\pi\pi^*$)
o-MMC	4.035	4.494	4.680	3.680	3.635	4.258
m-MMC	4.089	4.559	4.708	3.798	3.835	4.256
p-MMC	4.287	4.593	4.738	4.093	3.894	4.601

states of MMCs is different from OM*p*CA, where 2A′($^1\pi\pi^*$) is S_2 in vertical excitation.[21]

We then calculated the energies of $S_1(\pi\pi^*)$ and 1A″ ($^1n\pi^*$) of *p*-MMC and *p*-MMC-H_2O complexes and assessed the $S_1(\pi\pi^*) \rightarrow 1A''(^1n\pi^*)$ IC route by interpolating the energies between them (LIICs). The internal coordinate of an intermediate structure is given by changing the ratio(c) from 1.0 to 0.0 as follows:

$$\underline{R}(\text{LIIC}) = c \cdot \underline{R}_{\text{opt}}(S_1) + (1-c) \cdot \underline{R}_{\text{opt}}(^1n\pi^*), \quad (1)$$

where $\underline{R}_{\text{opt}}(S_1)$ is $S_1(\pi\pi^*)$-optimized internal coordinate and $\underline{R}_{\text{opt}}(^1n\pi^*)$ is the $^1n\pi*$-optimized internal coordinate. The calculated energy barrier of the IC route is possibly overestimated with this approximation.

Fig. 8 shows the LIIC plot of *s-cis/anti p*-MMC (black) and isomer **A** of *s-cis/anti p*-MMC-H_2O (red). Similar LIIC plot is obtained for isomer B of *s-cis/anti p*-MMC-H_2O (see Fig. S8 of the supplementary material for the LIIC plot[34]). The Cartesian coordinates for the structural changes are given in supplementary material (see Tables S1–S3 of the supplementary material[34]). As mentioned above, the adiabatic $^1n\pi^*$ state becomes the lowest, making the $S_1(\pi\pi^*) \rightarrow {}^1n\pi^*$ IC accessible. The energy barrier at the $S_1/{}^1n\pi^*$ potential crossing of *p*-MMC is 0.0483 eV (390 cm^{-1}) with respect to the S_1 state, which describes the observed excess energy dependence of the S_1 lifetime. On the other hand, the calculation for the *p*-MMC-H_2O complex gives a conflict result

with the observation, because the hydration to the carbonyl group slightly lowers the energy of $S_1(\pi\pi^*)$ but raises the $^1n\pi^*$ state energy. The lowering of the $S_1(\pi\pi^*)$ energy in the complex reflects the spectral red-shit of the S_1-S_0 transition. The raise of the $^1n\pi^*$ state results in the large increases of the energy barrier of the $S_1/{}^1n\pi^*$ conical intersection, i.e., 0.216 eV (1742 cm^{-1}). If the IC is still favorable in the complex, the rate constant will be decelerated. However, we observed a shorter S_1 lifetime of the complex than the monomer. It indicates that the $S_1(\pi\pi^*) \rightarrow {}^1n\pi^*$ IC is not a major decay route when *p*-MMC forms a complex with water. In fact, Tan *et al.* did not acquire the electronic state assignable to the $^1n\pi^*$ state in the *p*-MMC-H_2O complex as well as the OM*p*CA-H_2O complex.[21,23]

C. Decay route along the twisting double bond in S_1

We examined another nonradiative decay route, which is twisting along the propenyl C=C double bond coordinate (*trans* → *cis* isomerization) on the S_1 surface. Fig. 9 shows the potential energy plot of (a) *p*-MMC and (b) *p*-MMC-H_2O calculated as a function of dihedral angle of the propenyl C=C bond. It should be noted that the CIS optimizations did not converge at the geometry with dihedral angle less than 135°. The S_1 potential energy of *p*-MMC increases as the dihedral angle decreases and reaches to the maxima at 150° that creates the barrier height of 0.020 eV (160 cm^{-1}).
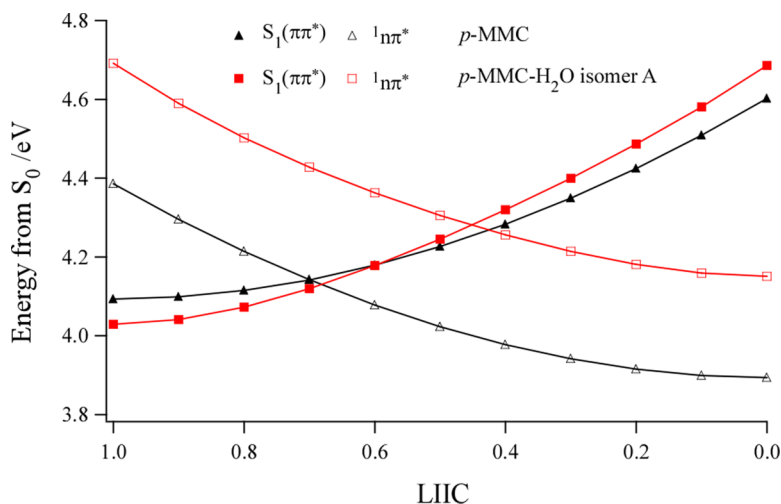

FIG. 8. The potential energy profiles along the $S_1(\pi\pi^*)$ and $^1n\pi^*$ coordinates of *s-cis/anti p*-MMC and isomer A of *s-cis/anti p*-MMC-H_2O calculated by TD-PBE0/cc-pVDZ. The horizontal-axis represents the structural change between the $S_1(\pi\pi^*)$ and $^1n\pi^*$ states, where the values 1.0 and 0.0 are the adiabatically optimized-$S_1(\pi\pi^*)$ energy level and adiabatically optimized-$^1n\pi^*$ energy level, respectively. The intermediate structure was obtained by translating the 3-dimensional internal coordinates and used to calculate the vertical excitation energy.
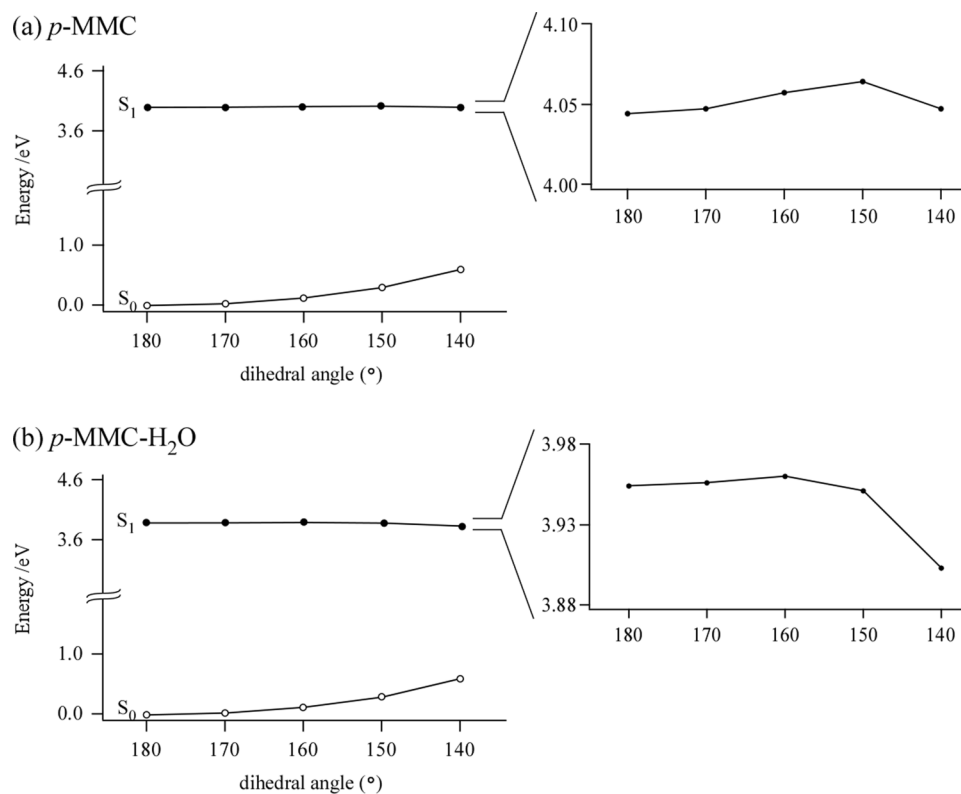
FIG. 9. Potential energy curves of the S_0 state (open circle) and the $S_1(\pi\pi^*)$ state (filled circle) for (a) *p*-MMC and (b) *p*-MMC-H$_2$O along the dihedral angle of the C = C bond. The energy of the S_1 state was calculated by CIS(D)/aug-cc-pVDZ, where the twisted structure at each angle was optimized by CIS/aug-cc-pVDZ. The ground state was calculated by MP2/aug-cc-pVDZ at the same structure.

On the other hand, the barrier height of the complex yields the 0.006 eV (48 cm^{-1}) at 160°, and the energy decreases as the dihedral angle decreases toward the isomerization. Therefore, it is suggested that the complex prefers the isomerizing decay in the $S_1(\pi\pi^*)$ state rather than the $S_1(\pi\pi^*) \rightarrow {}^1n\pi^*$ IC. It describes the observed shorter S_1 lifetime of the complex than the monomer and is consistent with the nanosecond laser study.[23] At this point, it is not clear whether the S_1 potential

curve intersects with the potential energy curve of S_0 leading to the isomerization to *cis*-isomer.

A remaining unanswered question is the observed conformer-specific S_1 lifetime of *p*-MMC. It may be understandable that the potential crossing between $S_1(\pi\pi^*)$ and ${}^1n\pi^*$ and the height of barrier along the twisting coordinate of double bond would be conformer dependent, so that the S_1 lifetime is different for different conformers. For example,
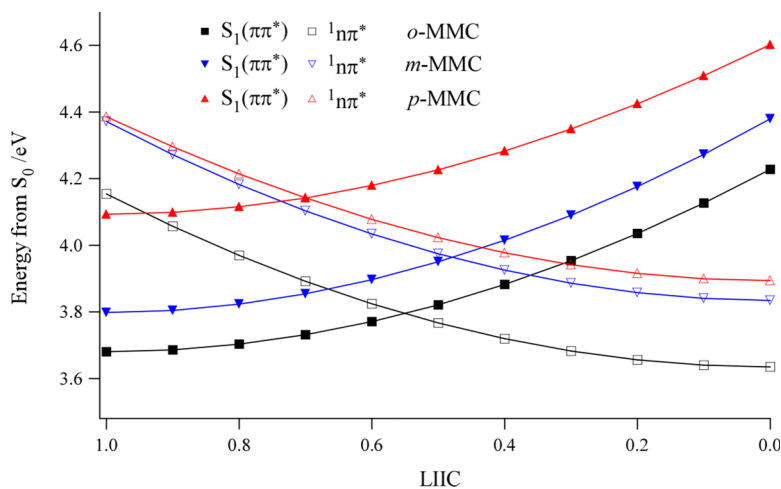

FIG. 10. The potential energy profiles along the $S_1(\pi\pi^*)$ and ${}^1n\pi^*$ coordinates of *o*-MMC (square, black), *m*-MMC (reversed triangle, blue), and *p*-MMC (triangle, red) calculated by TD-PBE0/cc-pVDZ. The horizontal-axis represents the structural change between the $S_1(\pi\pi^*)$ and ${}^1n\pi^*$ states, where the values 1.0 and 0.0 indicate the adiabatically optimized-$S_1(\pi\pi*)$ energy level and adiabatically optimized-${}^1n\pi^*$ energy level, respectively. The intermediate structure was obtained by changing the internal coordinate between them, which is used to calculate the vertical excitation energy.
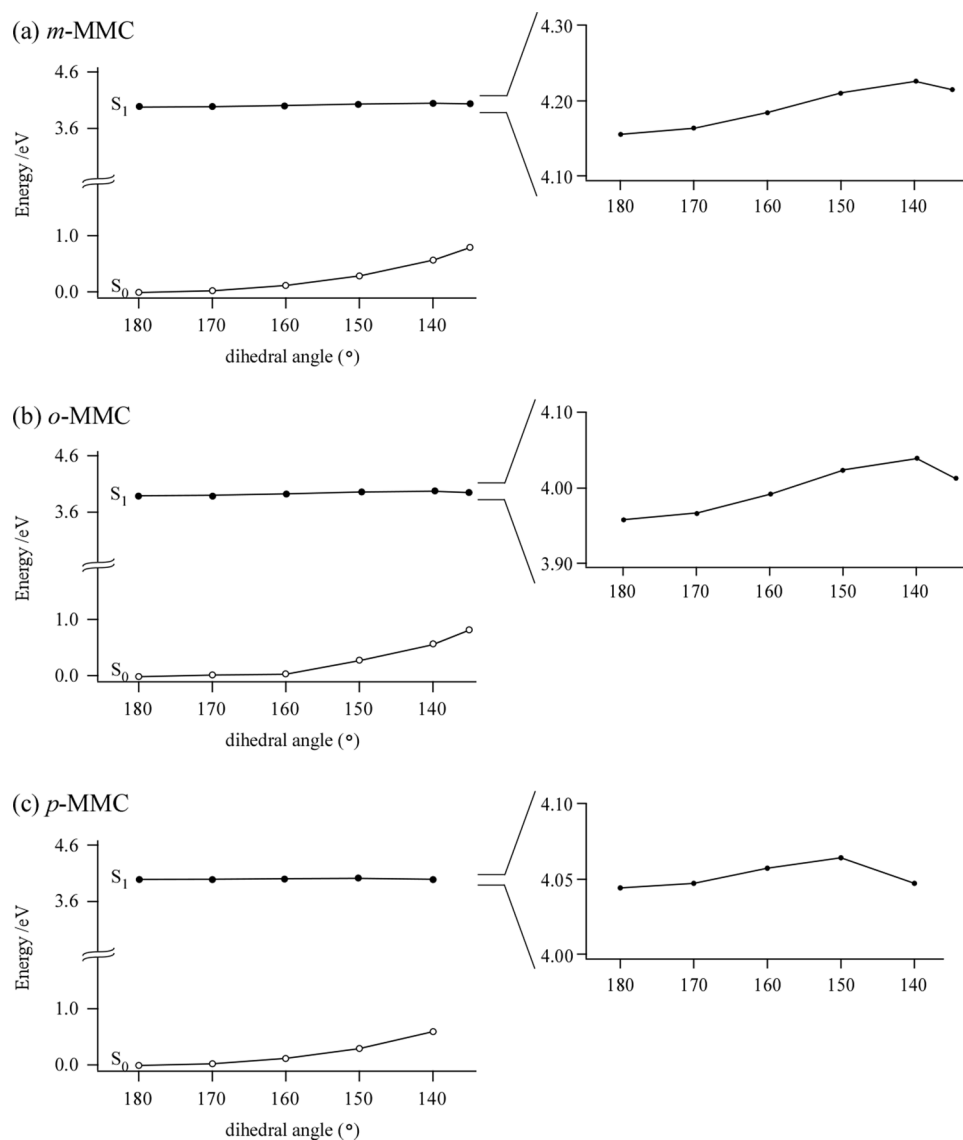
FIG. 11. Potential energy curves of the S_0 state (open circle) and the $S_1(\pi\pi^*)$ state (filled circle) for (a) *m*-MMC, (b) *o*-MMC, and (c) *p*-MMC along the dihedral angle of the C = C bond. The energy of the S_1 state was calculated by CIS(D)/aug-cc-pVDZ, where the twisted structure at each angle was optimized by CIS/aug-cc-pVDZ. The ground state was calculated by MP2/aug-cc-pVDZ at the same structure.

Mališ *et al.*[32,33] reported different S_1 state lifetimes for different conformers for peptides. At present, we did not have a reasonable description to answer why the decay rate constants of the conformers having higher energy transitions exhibit the shorter S_1 lifetimes. Since *s-cis/anti* conformer exhibits sharp increase of its decay rate constant within 150 cm^{-1} above the origin, the barrier of the nonradiative process is thought to be located at a few hundreds cm^{-1}. This barrier height is in good agreement with the theoretical prediction.

D. Nonradiative decay route of *m*– MMC and *o*-MMC

The same excited-state calculations as above were carried out for *o*- and *m*-MMCs. The experimental results suggest that neither the $S_1(\pi\pi^*) \rightarrow {}^1n\pi^*$ IC channel nor the isomerization channel is available. In Fig. 10, the $S_1(\pi\pi^*) \rightarrow {}^1n\pi^*$ IC route was examined by interpolating the energies between two states. The vertical excitation energies to the $S_1(\pi\pi^*)$ state for *o*-MMC

(black, 3.7 eV) and *m*-MMC (blue, 3.8 eV) are lower than *p*-MMC (4.1 eV), which agree with the experimental results. Their adiabatic energies of the ${}^1n\pi^*$ state are nearly equal to or higher than that of the $S_1(\pi\pi^*)$ state, which generates the energy barrier of 0.115 eV (928 cm^{-1}) for *o*-MMC and 0.164 eV (1320 cm^{-1}) for *m*-MMC. These values are twice or three times larger than 0.0483 eV (390 cm^{-1}) of *p*-MMC. Thus, $S_1(\pi\pi^*) \rightarrow {}^1n\pi^*$ IC route is unlikely to occur in these species. The potential energy curve along the double-bond twisting was also calculated as shown in Fig. 11. The energy barrier is estimated to be 0.081 eV (653 cm^{-1}) for *o*-MMC and 0.070 eV (565 cm^{-1}) for *m*-MMC. Both barrier heights are again much higher than that of *p*-MMC, suggesting that the nonradiative route is prohibited near the S_1-S_0 transition energy region. Therefore, the calculation describes the experimental result that neither $S_1(\pi\pi^*) \rightarrow {}^1n\pi^*$ IC route nor double-bond twisting decay route is accessible for these species, leading to the observed long S_1 lifetimes.

V. CONCLUSION

We recorded the S_1-S_0 electronic spectra (R2PI and LIF) of jet-cooled MMCs in the gas phase. UV-UV HB spectroscopy allowed us to find a number of conformers coexist in their excitation spectra. The lifetime measurement among MMCs confirmed the decisive position-dependence of the decay dynamics; *o*-MMC and *m*-MMC show relatively long S_1 lifetime on ns time scale with little conformer and excess energy dependence, while *p*-MMC exhibits S_1 lifetime on ps time scale with obvious conformer and excess energy dependencies. The UV and IR spectroscopic studies of *p*-MMC-H_2O provided the evidence of the complex structure where the water moiety is bound to the carbonyl oxygen, and the lifetime measurement revealed that the hydrogen-bond formation at the carbonyl group accelerates the nonradiative decay. The important remark on this article is the achievement of our electronic excited state calculations that describe the experimental observations. Two nonradiative decay routes are available via IC and isomerization in *p*-MMC, while *p*-MMC-H_2O decays via isomerization as hydration raises the energy level of the $n\pi^*$ state and inhibits the IC route. Both *m*-MMC and *o*-MMC decay radiatively because their energy barriers created by potential crossing and double-bond twisting are both too high to permit nonradiative decay.

ACKNOWLEDGMENTS

[1]A. L. Schilmiller, J. Stout, J. K. Weng, J. Humphreys, M. O. Ruegger, and C. Chapple, Plant J. **60**, 771 (2009).

[2]J. Kapteyn, A. V. Qualley, Z. Xie, E. Fridman, N. Dudareva, and D. R. Gang, Plant Cell **19**, 3212 (2007).

[3]R. Vanholme, B. Demedts, K. Morreel, J. Ralph, and W. Boerjan, Plant Physiol. **153**, 895 (2010).

[4]C. P. Rodrigo, W. H. James, and T. S. Zwier, J. Am. Chem. Soc. **133**, 2632 (2011).

[5]Y. Wang, M. Chantreau, R. Sibout, and S. Hawkins, Front. Plant Sci. **4**, 1 (2013).

[6]C. P. Vance, T. K. Kirk, and R. T. Shrwood, Annu. Rev. Phytopathol. **18**, 259 (1980).

[7]H. S. Abreu, J. V. F. Latorraca, R. P. W. Pereira, M. B. O. Monteiro, F. A. Abreu, and K. F. Amparado, An. Acad. Bras. Cienc. **81**, 137 (2009).

[8]B. Narasimhan, D. Belsare, D. Pharande, V. Mourya, and A. Dhake, Eur. J. Med. Chem. **39**, 827 (2004).

[9]S. E. Sattler and D. Funnel-Harris, Front. Plant Sci. **4**, 1 (2013).

[10]S. Prateek, J. Chem. Pharm. Res. **3**(2), 403 (2011).

[11]J. Hailing, C. Eleonora, B. Paul, P. Adrian, M. Frank, J. Jonathon, T. Chiara, W. Bernd, and M. Cathie, EMBO J. **19**, 6150 (2000).

[12]W. J. Zhang and L. O. Björn, Fitoterapia **80**, 207 (2009).

[13]S. Pattanaargson and P. Limphong, Int. J. Cosmetic Sci. **23**, 153 (2001).

[14]S. Pattanaargson, T. Munhapol, P. Hirunsupachot, and P. Luangthongaram, J. Photochem. Photobiol., A **161**, 269 (2004).

[15]T. M. Karpkird, S. Wanichweacharungruang, and B. Albinsson, Photochem. Photobiol. Sci. **8**, 1455 (2009).

[16]T. S. Singh and S. Mitra, Photochem. Photobiol. Sci. **7**, 1063 (2008).

[17]A. Le Person, A. S. Lacoste, and J. P. Cornard, J. Photochem. Photobiol., A **265**, 10 (2013).

[18]T. Ishigami, K. Nakazato, M. Uehara, and T. Endo, Tetrahedron Lett. **20**, 863 (1979).

[19]M. Promkatkaew, S. Suramitr, T. M. Karpkird, S. Namuangruk, and M. Ehara, J. Chem. Phys. **131**, 224306 (2009).

[20]M. Promkatkaew, S. Suramitr, T. Karpkird, S. Wanichwecharungruang, M. Ehara, and S. Hannongbua, Photochem. Photobiol. Sci. **13**, 583 (2014).

[21]E. M. M. Tan, S. Amirjalayer, B. H. Bakker, and W. J. Buma, Faraday Discuss. **163**, 321 (2013).

[22]D. Shimada, R. Kusaka, Y. Inokuchi, M. Ehara, and T. Ebata, Phys. Chem. Chem. Phys. **14**, 8999 (2012).

[23]E. M. M. Tan, M. Hilbers, and W. J. Buma, J. Phys. Chem. Lett. **5**, 2464 (2014).

[24]E. V. Gromov, I. Burghardt, H. Köppel, and L. S. Cederbaum, J. Phys. Chem. A **109**, 4623 (2005).

[25]E. M. M. Tan, S. Amirjalayer, P. Mazzella, B. H. Bakker, J. H. van Maarseveen, H. Bieraugel, and W. J. Buma, J. Phys. Chem. B **118**, 12395 (2014).

[26]T. N. V. Karsili, B. Marchetti, M. N. R. Ashfold, and W. Domcke, "*Ab initio* study of potential ultrafast internal conversion routes in oxybenzone, caffeic acid, and ferulic acid: Implications for sunscreens," J. Phys. Chem. A (published online).

[27]M. J. Frisch, G. W. Trucks, H. B. Schlegel, G. E. Scuseria, M. A. Robb, J. R. Cheeseman, G. Scalmani, V. Barone, B. Mennuchi, G. Petersson *et al.*, Gaussian 09, Gaussian Inc., Wallingford, CT, 2010.

[28]C. Adamo and V. Barone, J. Chem. Phys. **110**, 6158 (1999).

[29]T. H. Dunning, Jr., J. Chem. Phys. **90**, 1007 (1989).

[30]M. Head-Gordon, R. J. Rico, M. Oumi, and T. J. Lee, Chem. Phys. Lett. **219**, 21 (1994).

[31]V. P. Barber and J. J. Newby, J. Phys. Chem. A **117**, 12831 (2013).

[32]M. Mališ, Y. Loquais, E. Gloaguen, H. S. Biswal, F. Piuzzi, B. Tardivel, V. Brenner, M. Broquier, C. Jouvet, M. Mons, N. Došlić, and I. Ljubić, J. Am. Chem. Soc. **134**, 20340 (2012).

[33]M. Mališ, Y. Loquais, E. Gloaguen, C. Jouvet, V. Brenner, M. Mons, and N. Došlić, Phys. Chem. Chem. Phys. **16**, 2285 (2014).

[34]See supplementary material at http://dx.doi.org/10.1063/1.4904268 for sample preparation, for possible conformations of *m*-MMC and *o*-MMC (Fig. S1), for the structures and IR spectra of possible isomers of the *s-cis/anti p*-MMC-H_2O complex (Figs. S2 and S3), for the geometrical changes of the S_1, S_2, and S_3 states relative to S_0 for *o*-MMC, *m*-MMC, and *p*-MMC (Figs. S4–S6), for potential energy profiles of $1A'^1\pi\pi^*$, $1A''^1n\pi^*$, and $2A'^1\pi\pi^*$ vs. LIIC coordinate of *s-cis/anti p*-MMC (Fig. S7), for potential energy profiles of $1A'^1\pi\pi^*$ and $1A''^1n\pi^*$ vs. LIIC coordinate for *s-cis/anti p*-MMC and isomers A and B of *s-cis/anti p*-MMC-H_2O (Fig. S8), and Cartesian coordinates of *s-cis/anti p*-MMC, isomer A of *s-cis/anti p*-MMC-H_2O, and isomer B of *s-cis/anti p*-MMC-H_2O at different values of ratio for LIIC calculation (Tables S1-S3).